

QUERY FORM

JOURNAL: The Astrophysical Journal

AUTHOR: Brandenburg et al.

TITLE: Magnetorotational Instability in a Solar Near-surface Mean-field Dynamo

ARTICLE ID: apj03c4

Page 1

Q1
Your article has been processed in line with the journal style. Your changes will be reviewed by the Production Editor, and any amendments that do not comply with journal style or grammatical correctness will not be applied and will not appear in the published article.

Page 1

Q2
The layout of this article has not yet been finalized. This proof may contain columns that are not fully balanced/matched or other typographical imperfections; these issues will be resolved once the final corrections have been incorporated.

Page 1

Q3
Please check that the **names of all authors as displayed in the proof are correct**, and that all **authors are linked to the correct affiliations**. Please also confirm that the correct corresponding author has been indicated. **Note that this is your last opportunity to review and amend this information before your article is published.**

Page 1

Q4
We have been provided with ORCID iDs for the authors as below. Please confirm whether the numbers are correct.
Axel Brandenburg 0000-0002-7304-021X
Gustav Larsson 0009-0008-4918-3852
Fabio Del Sordo 0000-0001-9268-4849
Petri J. Käpylä 0000-0001-9619-0053

Page 1

Q5
Please confirm typesetting of 'shearing-periodic box' here and elsewhere in the paper, i.e. as a hyphenated compound. Should this be styled with an en dash, i.e. as an (x,y) relation?

Page 1

Q6
Please confirm rephrasing of 'tends to go' to 'occurs' in '[...] which occurs at the expense of the magnetic energy.'

Page 1

Q7
Please confirm slight rephrasing of 'In addition to the Sun and other stars, proto-neutron stars represent a particularly prominent application'. In addition, by 'prominent' do you mean 'common'/'widespread'? or 'important' in the sense of 'significant'?

Page 2

Q8

Please confirm styling of 'incoherent α -shear effect'. Should this be a hyphenated compound, i.e. the same as shear-current effect', or an en dash relation, i.e. between the alpha effect and shear?

Page 2

Q9

Please confirm usage of 'top-bottom symmetry'. Would 'top-down symmetry' be more appropriate in this context? Or is top-bottom an accepted nomenclature in the field?

Page 2

Q10

Please confirm phrasing of 'However, such a description can only be an effective one, because the level of turbulence is unknown ...' Do you mean 'can only be an approximate one'?

Page 9

Q11

Please check phrasing of 'To decide about the excitation of the MRI, ...' Would it be better to say something like 'To further assess their excitation of the MRI ...'? Or, to continue with the sense of 'decide', 'To help determine whether or not MRI was excited in their study ...'?

Page 10

Q12

If you have an Acknowledgments section, please check that the information there is complete and correct and that all relevant institutions, grant numbers, programs, and collaborators are mentioned as appropriate.

Page 11

Q13

Please check the details for any journal references that do not have a link; please update with correct details and supply a CrossRef DOI or NASA ADS link if available.

Page 11

Q14

Please update if possible all references where only the arXiv preprint number is given.



Magnetorotational Instability in a Solar Near-surface Mean-field Dynamo

Axel Brandenburg^{1,2,3,4} , Gustav Larsson^{1,5} , Fabio Del Sordo^{6,7} , and Petri J. Käpylä⁸

¹ Nordita, KTH Royal Institute of Technology and Stockholm University, Hannes Alfvéns väg 12, 10691 Stockholm, Sweden
² The Oskar Klein Centre, Department of Astronomy, Stockholm University, AlbaNova, 10691 Stockholm, Sweden
³ McWilliams Center for Cosmology & Department of Physics, Carnegie Mellon University, Pittsburgh, PA 15213, USA
⁴ School of Natural Sciences and Medicine, Ilia State University, 3-5 Cholokashvili Avenue, 0194 Tbilisi, Georgia
⁵ Department of Physics, Stockholm University, AlbaNova, 10691 Stockholm, Sweden
⁶ Scuola Normale Superiore, Piazza dei Cavalieri, 7 56126 Pisa, Italy
⁷ INAF, Osservatorio Astrofisico di Catania, via Santa Sofia, 78 Catania, Italy
⁸ Institut für Sonnenphysik (KIS), Georges-Köhler-Allee 401a, 79110 Freiburg im Breisgau, Germany

Received 2025 April 23; revised 2025 August 28; accepted 2025 August 30; published 2025 MM DD

Abstract

We address the question whether the magnetorotational instability (MRI) can operate in the near-surface shear layer (NSSL) of the Sun and how it affects the interaction with the dynamo process. Using hydromagnetic mean-field simulations of $\alpha\Omega$ -type dynamos in rotating shearing-periodic boxes, we show that for negative **shear** the MRI can operate above a certain critical shear parameter. This parameter scales inversely with the equipartition magnetic field strength above which α quenching set in. Like the usual Ω effect, the MRI produces toroidal magnetic field when the field is sufficiently strong. The work done by the Lorentz force is positive, so the magnetic field drives kinetic energy and not the other way around, as in a turbulent dynamo. This results in strong kinetic energy production and dissipation, which **occurs** at the expense of the magnetic energy. In view of the application to the solar NSSL, we conclude that the turbulent magnetic diffusivity may be too large for the MRI to be excited and that therefore only the standard Ω effect is expected to operate.

Unified Astronomy Thesaurus concepts: **Magnetic fields** (994)

1. Introduction

The magnetorotational instability (MRI) provides a source of turbulence in accretion **disks**, where it feeds on Keplerian shear to turn potential energy into kinetic and magnetic energies; see S. A. Balbus & J. F. Hawley (1998) for a review. For the MRI to be excited, the angular velocity Ω must decrease with increasing distance ϖ from the rotation axis, i.e., $\partial\Omega/\partial\varpi < 0$. There must also be a moderately strong magnetic field. This condition is obeyed not only in accretion **disks**, but also in stars like the Sun, where both requirements may be satisfied in the **near-surface** shear layer (NSSL), the outer 4% of the solar radius (J. Schou et al. 1998). This motivated G. M. Vasil et al. (2024) to study the excitation properties of the MRI in the NSSL of the Sun using spherical global modes.

The possible relevance of the MRI for stellar radiative zones has been discussed for a long time (S. A. Balbus & J. F. Hawley 1994; V. A. Urpin 1996; K. Menou et al. 2004). K. P. Parfrey & K. Menou (2007) proposed that small-scale magnetorotational turbulence prevents coherent magnetic dynamo action in the tachocline at higher latitudes. They argued that this could explain the latitudinal restriction of solar active regions to the vicinity of the equator. Y. Masada (2011) suggested that the MRI could play a role in maintaining thermal wind balance in the Sun. D. Kagan & J. C. Wheeler (2014) found that nonaxisymmetric MRI modes tend to grow faster in the Sun than the corresponding axisymmetric modes. J. C. Wheeler et al. (2015) found the MRI to play a role in the later stages of massive star evolution. Unlike the recent work by G. M. Vasil et al. (2024), these papers only considered local

analyses. In addition to the Sun and other stars, proto-neutron stars **represent** a particularly prominent **application** (A. Reboul-Salze et al. 2022).

In the **Sun's** outer 30% by radius there is convection converting part of the **Sun's** thermal energy into kinetic energy. The nonuniform rotation of the Sun is explained by the fact that the convection is anisotropic such that solid-body rotation is no longer a solution to a rotating fluid even in the absence of external torques (A. I. Lebedinskii 1941; J. Wasitynski 1946; R. Kippenhahn 1963; H. Köhler 1970; G. Rüdiger 1980; A. Brandenburg et al. 1990). This causes also the emergence of the aforementioned NSSL (G. Rüdiger et al. 2014; L. L. Kitchatinov 2016, 2023). In addition, small-scale (M. Meneguzzi & A. Pouquet 1989; A. Nordlund et al. 1992; A. Brandenburg et al. 1996; F. Cattaneo 1999) and large-scale (P. J. Käpylä et al. 2008; D. W. Hughes & M. R. E. Proctor 2009; Y. Masada & T. Sano 2014; P. J. Bushby et al. 2018) magnetic fields **exist** as a result of the convective turbulence. The presence of radial stratification in density **and/or** turbulent intensity, together with global rotation, causes the occurrence of large-scale magnetic fields (H. K. Moffatt 1978; E. N. Parker 1979; F. Krause & K.-H. Rädler 1980; Y. B. Zeldovich et al. 1983). Thus, in the Sun, the two ingredients of the MRI—differential rotation and magnetic fields—are ultimately caused by the underlying convection.

G. M. Vasil et al. (2024) argue that an initial poloidal magnetic field is only present at the start of the cycle to get the MRI excited. Furthermore, they argue that the MRI itself is important in driving the dynamo process. However, the magnetic field required to sustain the MRI **must** come from a dynamo process and cannot rely on the initial field. To address the question of whether or not the MRI is excited and whether it contributes to shaping the **Sun's** magnetic field to display equatorward migration of a global large-scale magnetic



Original content from this work may be used under the terms of the **Creative Commons Attribution 4.0 licence**. Any further distribution of this work must maintain attribution to the author(s) and the title of the work, journal citation and DOI.

field, we need to separate the MRI-driven flows from the convection. One approach is to ignore convection but to retain some of its secondary effects, i.e., the NSSL with $\partial\Omega/\partial\varpi < 0$ and magnetic fields; see the discussion by G. M. Vasil et al. (2024) and an appraisal by E. Zweibel (2024). Another approach, the one taken here, is to average over the convection. By employing azimuthal averages, one is left with a stationary, nonturbulent background. Furthermore, correlations among different components of the fluctuating parts of the turbulent velocity and magnetic fields emerge that are parameterized in terms of (i) diffusive contributions, such as turbulent viscosity and turbulent magnetic diffusion, and (ii) nondiffusive contributions such as Λ and α effects. There is no universal agreement about the relevance of these effects (e.g., H. C. Spruit 2011; D. W. Hughes 2018). In the mean-field description of the Sun, they are crucial effects able to explain the production of differential rotation and large-scale magnetic fields (G. Rüdiger & R. Hollerbach 2004). These effects can explain the NSSL and the large-scale magnetic field by solving the averaged form of the underlying equations (V. V. Pipin 2017); see A. Brandenburg et al. (2023) for a review.

Apart from the α effect, there are also several other mean-field effects that can produce large-scale magnetic fields: turbulent pumping with a time delay, negative turbulent magnetic diffusivity, the Rädler effect, the shear-current effect, and the incoherent α -shear effect; see Table 2 of A. Brandenburg & E. Ntormousi (2023). In addition, in phenomenological studies of solar magnetism, the decay of active regions is sometimes associated with a dynamo effect (R. B. Leighton 1969). In its simplest form, however, it is just an α effect (M. Stix 1974). In a more advanced formulation, it can be written as a nonlocal α effect; see M. Dikpati & P. Charbonneau (1999) for an example implementation in a mean-field model, and A. Brandenburg & P. J. Käpylä (2007) for results regarding the effect on magnetic helicity conservation in the Sun. In any case, it would not be possible to adopt such an effect here due to the top-bottom symmetry of our model.

It is possible to study the interaction between the MRI and the dynamo in fully three-dimensional turbulence simulations. However, the essentials of these processes may well be captured in a mean-field approach. Using direct numerical simulations with forced turbulence, M. S. Väisälä et al. (2014) demonstrated that the onset of the MRI is consistent with what is expected from mean-field estimates. In particular, the onset requires larger magnetic Reynolds numbers than in the ideal case due to the action of turbulent diffusion.

Averaging over the convective motions of the Sun has been done previously in the context of mean-field hydrodynamics with the Λ effect. When including compressibility and thermodynamics, it was noticed that the equations display an instability (P. J. Gierasch 1974; W. Schmidt 1982; K. L. Chan et al. 1987; G. Rüdiger & I. Tuominen 1991; G. Rüdiger & F. Spahn 1992) whose nature was not initially understood. However, this later turned out to be an example where averaging over the convection leads to mean-field equations that themselves are susceptible to an instability, namely the onset of convection. This depends on how close the mean-field state is to adiabatic and on the values of the turbulent viscosity and turbulent thermal diffusivities (I. Tuominen et al. 1994).

When magnetic fields are present and sustained by a dynamo, the full system of magnetohydrodynamic equations

may be unstable to the MRI. We must emphasize that we are here not talking about the previously studied case where the MRI provides the source of turbulence, which then reinforces an initial magnetic field by dynamo action through a self-sustained doubly positive feedback cycle (A. Brandenburg et al. 1995; J. F. Hawley et al. 1996; J. M. Stone et al. 1996). Even in that case, a mean-field description may be appropriate to quantify the nature of a large-scale dynamo governed by rotation and stratification (A. Brandenburg & D. Sokoloff 2002; A. Brandenburg 2005a; O. Gressel 2010). However, such a description can only be an effective one, because the level of turbulence is unknown and emerges only when solving the underlying, essentially nonlinear dynamo problem (F. Rincon et al. 2007; G. Lesur & G. I. Ogilvie 2008; J. Herauld et al. 2011).

In the present paper, we focus on the simpler case where a mean-field dynamo is assumed to exist but may be modified by the MRI. Ideally, in view of solar applications, it would be appropriate to consider an axisymmetric hydromagnetic mean-field dynamo with differential rotation being sustained by the Λ effect. Such systems have been studied for a long time (A. Brandenburg et al. 1990, 1991, 1992; L. L. Kitchatinov & G. Rüdiger 1995; M. Rempel 2006; V. V. Pipin 2017; V. V. Pipin & A. G. Kosovichev 2019), but no MRI was ever reported in such studies. One reason for this might be that it is hard to identify the operation of the MRI in a system that is already governed by a strong instability responsible for producing the magnetic field. We therefore take a step back and consider here a system in Cartesian geometry. In Section 2, we provide the details of our model, and present the results in Section 3. We conclude in Section 4.

2. Our Model

2.1. Shearing Box Setup

Following the early work of S. A. Balbus & J. F. Hawley (1991, 1992) and J. F. Hawley & S. A. Balbus (1991, 1992), we study the MRI in a shearing-periodic box, where x is the cross-stream direction, y is the streamwise or azimuthal direction, and z is the spanwise or vertical direction. As in M. S. Väisälä et al. (2014), we consider the mean-field equations for azimuthally averaged velocities $\bar{U}(x, z, t)$, the magnetic field $\bar{B}(x, z, t)$, and the mean density $\bar{\rho}(x, z, t)$. The system is rotating with angular velocity Ω , and there is a uniform shear flow $\bar{V}(x) = (0, Sx, 0)$, so the full velocity is therefore given by $\bar{V} + \bar{U}$. We consider the system to be isothermal with constant sound speed c_s , so the mean pressure $\bar{p}(x, z, t)$ is given by $\bar{p} = \bar{\rho}c_s^2$. The mean magnetic field is expressed in terms of the mean magnetic vector potential $\bar{A}(x, z, t)$ with $\bar{B} = \nabla \times \bar{A}$ to satisfy $\nabla \cdot \bar{B} = 0$. The full system of equations for $\bar{\rho}$, \bar{U} , and \bar{A} is given by (A. Brandenburg et al. 1995, 2008)

$$\frac{D \ln \bar{\rho}}{Dt} = -\nabla \cdot \bar{U}, \quad (1)$$

$$\begin{aligned} \frac{D\bar{U}}{Dt} = & -S\bar{U}_x\hat{y} - 2\Omega \times \bar{U} - c_s^2 \nabla \ln \bar{\rho} \\ & + [\bar{J} \times \bar{B} + \nabla \cdot (2\nu_T \bar{\rho} \bar{S})]/\bar{\rho}, \end{aligned} \quad (2)$$

$$\frac{\partial \bar{A}}{\partial t} = -S\bar{A}_y\hat{x} + \bar{U} \times \bar{B} + \alpha \bar{B} - \eta_T \mu_0 \bar{J}, \quad (3)$$

where $D/Dt = \partial/\partial t + \bar{\mathbf{U}} \cdot \nabla$ is the advective derivative, $\bar{\mathbf{S}}$ is the rate-of-strain tensor of the mean flow with the components $\bar{S}_{ij} = (\partial_i \bar{U}_j + \partial_j \bar{U}_i)/2 - \delta_{ij} \nabla \cdot \bar{\mathbf{U}}/3$, $\bar{\boldsymbol{\Omega}}$ is the angular velocity, $S = -q\Omega$ is the shear parameter, and $\bar{\mathbf{J}} = \nabla \times \bar{\mathbf{B}}/\mu_0$ is the mean current density with μ_0 being the vacuum permeability. There are three mean-field parameters: the turbulent viscosity ν_T , the turbulent magnetic diffusivity η_T , and the α effect. Note that in our two-dimensional case, $\bar{\mathbf{V}} \cdot \nabla = Sx\partial_y = 0$. In some cases, we allow for α quenching and write

$$\alpha = \alpha_0/(1 + \bar{\mathbf{B}}^2/B_{\text{eq}}^2), \quad (4)$$

where B_{eq} is the equipartition field strength above which α begins to be affected by the feedback from the Lorentz force of the small-scale magnetic field (T. S. Ivanova & A. A. Ruzmaikin 1977). We sometimes refer to this as microphysical feedback to distinguish it from the macrophysical feedback from the Lorentz force of the large-scale magnetic field, $\bar{\mathbf{J}} \times \bar{\mathbf{B}}$. This type of saturation is sometimes also called the Malkus–Proctor mechanism, after the early paper by W. V. R. Malkus & M. R. E. Proctor (1975), who employed spherical geometry.

In the absence of α quenching ($B_{\text{eq}} \rightarrow \infty$), the only possibility for the dynamo to saturate is via the Lorentz force from the mean magnetic field, $\bar{\mathbf{J}} \times \bar{\mathbf{B}}$, i.e., the aforementioned Malkus–Proctor mechanism. Also relevant to our present work is that of M. Schüssler (1979), who considered Cartesian geometry. Our solutions, however, are simpler still in that we employ periodic boundary conditions in most cases.

A simple way to identify the operation of the MRI in a dynamo is by comparing models with positive and negative values of q , because the MRI only works in the range $0 < q < 2$. Note also that for $q > 2$, the hydrodynamic state is Rayleigh unstable and results in an exponentially growing shear flow, $\bar{U}_y(z)$, without ever saturating in a periodic system. For the solar NSSL, however, we have $q = 1$ (A. Barekat et al. 2014).

Given that our main interest lies in the investigation of the effect of the MRI on a dynamo, where any value of q in the range $0 < q < 2$ is of interest, we have chosen here $q = 3/2$ for Keplerian accretion disks. Smaller values of q reduce the stress by a factor $q/(2 - q)$ (M. Abramowicz et al. 1996), but the MRI is qualitatively unchanged. Below, we demonstrate with a few runs that this is true for most quantities. Obviously, for proper predictions for the Sun and Sun-like stars, not only $q = 1$ but also proper spherical geometry must be used. Finally, as motivated above, we also consider negative values of q .

Some of our models with positive shear ($S > 0$ or $q < 0$), where the MRI is inactive, do not saturate in the absence of α quenching. To check whether this is a peculiarity of the use of periodic boundary conditions, we also consider models with what is called a vertical field condition, i.e.,

$$\bar{B}_x = \bar{B}_y = \partial_z \bar{B}_z = 0, \quad (5)$$

which corresponds to $\partial_z \bar{A}_x = \partial_z \bar{A}_y = \bar{A}_z = 0$. Note that with this boundary condition the normal component of the Poynting vector $\bar{\mathbf{E}} \times \bar{\mathbf{B}}/\mu_0$, where $\bar{\mathbf{E}} = \eta_T \mu_0 \bar{\mathbf{J}} - \bar{\mathbf{U}} \times \bar{\mathbf{B}}$ is the mean electric field, vanishes. Thus, energy conservation is still preserved.

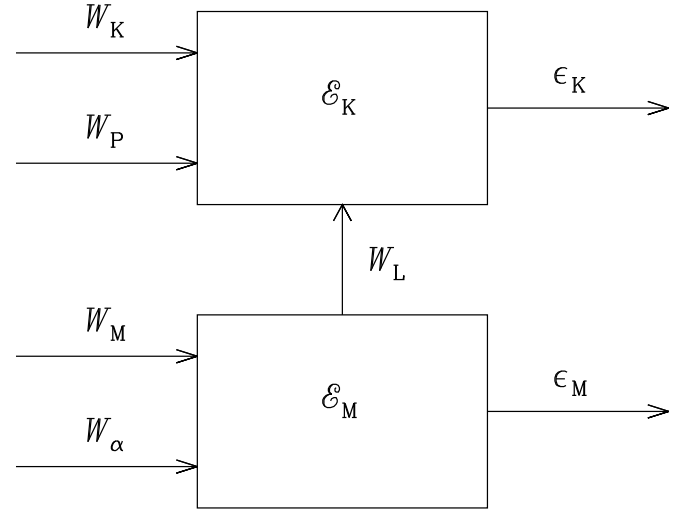


Figure 1. Flow of energy in a hydromagnetic mean-field dynamo.

2.2. Input and Output Parameters

We consider a two-dimensional domain $L_x \times L_z$, and define $k_1 = 2\pi/L_z$ as our reference wavenumber, which is the lowest wavenumber in the z -direction. The lowest wavenumber in the x -direction is $k_{1x} = 2\pi/L_x$. Our main input parameters are

$$C_\alpha = \alpha_0/\eta_T k_1, \quad C_\Omega = S/\eta_T k_1^2, \quad (6)$$

as well as $q = -S/\Omega$ and B_{eq} , which can be expressed via the corresponding Alfvén speed, $v_A^{\text{eq}} \equiv B_{\text{eq}}/\sqrt{\mu_0 \rho_0}$, in nondimensional form as

$$\mathcal{B}_{\text{eq}} \equiv v_A^{\text{eq}} k_1 / \Omega. \quad (7)$$

In all our cases, we assume $\text{Pr}_M \equiv \nu_T/\eta_T = 1$ for the turbulent magnetic Prandtl number. The sound speed is specified in terms of the ratio $C_s \equiv c_s k_1 / \Omega$, for which we take in most of the cases $C_s = 10$. As we will see below, the kinetic energy of the generated flows is typically well below $\rho_0 \Omega^2 / k_1^2$. Therefore, the value of $C_s = 10$ is large enough so that the results are not affected by compressibility effects—even in those cases where the kinetic energy exceeds $\rho_0 \Omega^2 / k_1^2$ by some amount.

The diagnostic output parameters are the energies of the mean fields that are derived either under yz or xy averaging, \mathcal{E}_M^x and \mathcal{E}_M^z , respectively. These are sometimes normalized by $\mathcal{E}_M^{\text{eq}} \equiv B_{\text{eq}}^2 / 2\mu_0$. We also monitor various parameters governing the flow of energy in our system. These include the mean kinetic and magnetic energy densities, $\mathcal{E}_K = \langle \bar{\rho} \bar{\mathbf{U}}^2 / 2 \rangle$ and $\mathcal{E}_M = \langle \bar{\mathbf{B}}^2 / 2\mu_0 \rangle$, their time derivatives, $\dot{\mathcal{E}}_K$ and $\dot{\mathcal{E}}_M$, the kinetic and magnetic energy dissipation rates, $\epsilon_K = \langle 2\bar{\rho} \nu_T \bar{\mathbf{S}}^2 \rangle$ and $\epsilon_M = \langle \eta_T \mu_0 \bar{\mathbf{J}}^2 \rangle$, the fluxes of kinetic and magnetic energy tapped from the shear flow, $W_K = \langle \bar{\rho} \bar{U}_x \bar{U}_y S \rangle$ and $W_M = -\langle \bar{B}_x \bar{B}_y S / \mu_0 \rangle$, the work done by the pressure force, $W_P = -\langle \bar{\mathbf{U}} \cdot \nabla \bar{p} \rangle$ as well as the work done by the α effect, $W_\alpha = \langle \alpha \bar{\mathbf{J}} \cdot \bar{\mathbf{B}} \rangle$, and the work done by the Lorentz force, $W_L = \langle \bar{\mathbf{U}} \cdot (\bar{\mathbf{J}} \times \bar{\mathbf{B}}) \rangle$. Figure 1 gives a graphical illustration showing the flow of energy in a hydromagnetic mean-field dynamo with shear.

For a uniform vertical magnetic field, $\mathbf{B}_0 = (0, 0, B_0)$, the MRI is excited when $v_{A0} k_1 < \sqrt{2\Omega S}$, where $v_{A0} = B_0 / \sqrt{\mu_0 \rho_0}$ is the Alfvén speed of the uniform vertical magnetic field. The MRI can be modeled in one dimension with $\nabla_x = (0, 0, \partial_z)$.

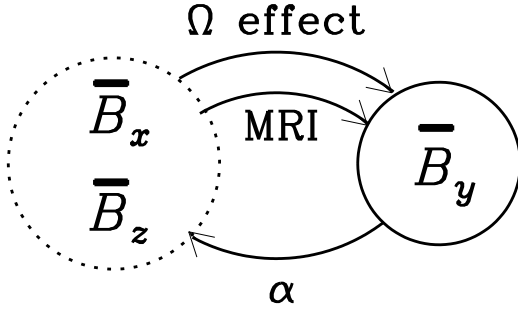


Figure 2. Sketch illustrating the generation of \bar{B}_y from \bar{B}_x through the Ω effect and from \bar{B}_z through the MRI, and the generation of both \bar{B}_x and \bar{B}_z from \bar{B}_y through the α effect.

Such a one-dimensional setup could also lead to what is called an $\alpha\Omega$ dynamo, which means that the mean radial or cross-stream field \bar{B}_x is regenerated by the α effect and the mean toroidal or streamwise field \bar{B}_y is regenerated by the Ω effect, or, more precisely, the shear flow $\bar{V}(x)$. One sometimes also talks about an α^2 dynamo if there is no shear, or about an $\alpha^2\Omega$ dynamo if both the α effect and shear contribute to regenerating \bar{B}_y .

In the one-dimensional case with $\nabla_z = (0, 0, \partial_z)$ and periodic boundary conditions, the α^2 dynamo is excited when $C_\alpha > 1$, while the $\alpha\Omega$ dynamo is excited for $C_\alpha C_\Omega > 2$ (A. Brandenburg & K. Subramanian 2005). Because of $\nabla \cdot \bar{\mathbf{B}} = 0$, the resulting magnetic field is then of the form $\bar{\mathbf{B}}(z) = (\bar{B}_x, \bar{B}_y, 0)$, i.e., $\bar{B}_z = 0$, so it is not possible for the MRI to be excited.

This would change if the dynamo also had an x extent. To see this, we consider for a moment a one-dimensional domain with $\nabla_x = (\partial_x, 0, 0)$. In that case, an α^2 dynamo with $\bar{\mathbf{B}}(x) = (0, \bar{B}_y, \bar{B}_z)$ can be excited, allowing $\bar{B}_z \neq 0$. It would be excited when $\alpha_0/\eta_T k_{1x} \equiv C_\alpha k_{1x}/k_{1x} > 1$, i.e., $C_\alpha > k_{1x}/k_1 = L_z/L_x$. Figure 2 gives a graphical illustration of the generation of \bar{B}_y from \bar{B}_x through the Ω effect and from \bar{B}_z through the MRI, and the generation of both \bar{B}_x and \bar{B}_z from \bar{B}_y through the α effect.

To allow for the possibility that in our two-dimensional domain such a dynamo is preferred over one with a z extent, we choose our domain to be oblate, e.g., $L_x/L_z = 2$. We solve the equations with the PENCIL CODE (Pencil Code Collaboration et al. 2021) using numerical resolutions between 64×128 and 256×512 mesh points, i.e., the mesh spacings in the x - and z -directions are kept the same.

2.3. Dynamo Types in the Rädler Diagram

It is convenient to discuss solutions in the C_α – C_Ω plane; see Figure 3. Such diagrams were extensively exploited by K. H. Rädler (1986), which is why we refer to such plots in the following as Rädler diagrams. Rädler considered dynamos in spherical geometry where α changed sign about the equator, so the solutions were either symmetric or antisymmetric about the equator. In addition, they could be axisymmetric or antisymmetric, and they could also be oscillatory or stationary.

For a one-dimensional $\alpha^2\Omega$ dynamo with periodic boundary conditions, the complex growth rate is $(\alpha^2 k^2 - i k \alpha S)^{1/2} - \eta_T k^2$ (A. Brandenburg & K. Subramanian 2005). For the marginally excited state, we require the real

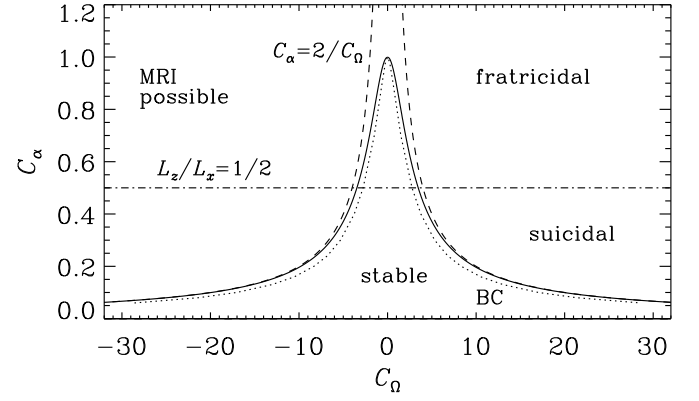


Figure 3. Rädler diagram for the $\alpha^2\Omega$ dynamo with z extent (solid line) and the α^2 dynamo with x extent in a domain with $L_z/L_x = 1/2$ (horizontal dashed-dotted line). The onset location in the pure $\alpha\Omega$ approximation ($C_\alpha C_\Omega = 2$) is shown as dashed lines. The case with the vertical field boundary condition is shown as the dotted line and is marked BC.

part of the complex growth rate to vanish. This yields

$$C_\Omega = C_\alpha \sqrt{(2/C_\alpha^2 - 1)^2 - 1}, \quad (8)$$

which is the solid line shown in Figure 3. For the vertical field boundary condition, the dynamo is slightly easier to excite; see the dotted line in Figure 3, which has been obtained numerically.

The Rädler diagram gives a graphical overview of the differences between dynamos with positive and negative shear, i.e., positive and negative values of C_Ω . The MRI is only possible for $C_\Omega < 0$ (negative shear), while for $C_\Omega > 0$, we just expect ordinary $\alpha\Omega$ dynamo waves. This expectation, however, does not apply to dynamos in periodic domains with $\alpha_0 = \text{const}$, as was first found in the fully three-dimensional turbulence simulations of A. Hubbard et al. (2011). Their $\alpha\Omega$ dynamo started off as expected, but at some point during the early, nonlinear saturation phase of \mathcal{E}_M^X , the dynamo wave stopped and a new solution emerged that had a cross-stream variation, i.e., \mathcal{E}_M^X became strong and suppressed \mathcal{E}_M^Z .

A similar type of exchange of dynamo solutions in the nonlinear regime was first found by H. Fuchs et al. (1999) while investigating hydromagnetic dynamos with Malkus–Proctor feedback in a sphere. They found self-killing and self-creating dynamos due to the presence of different stable flow patterns where the magnetic field causes the solution to respond to a newly emerged flow pattern after the initial saturation. This was thus the first example of what then became known as a suicidal dynamo.

In analogy with suicidal dynamos, the dynamos found by A. Hubbard et al. (2011) were called fratricidal dynamos. This property of dynamos in a periodic domain emerged as a problem because $\alpha\Omega$ dynamos in a periodic domain could only be studied for a limited time interval before they disappeared (B. B. Karak & A. Brandenburg 2016).

3. Results

We begin with a discussion of fratricidal and suicidal dynamos, but emphasize that these have so far only been found in periodic systems for $C_\Omega > 0$, i.e., for positive shear. Thus, to examine the effect of the MRI, we compare solutions with positive and negative values of C_Ω using both periodic and nonperiodic domains.

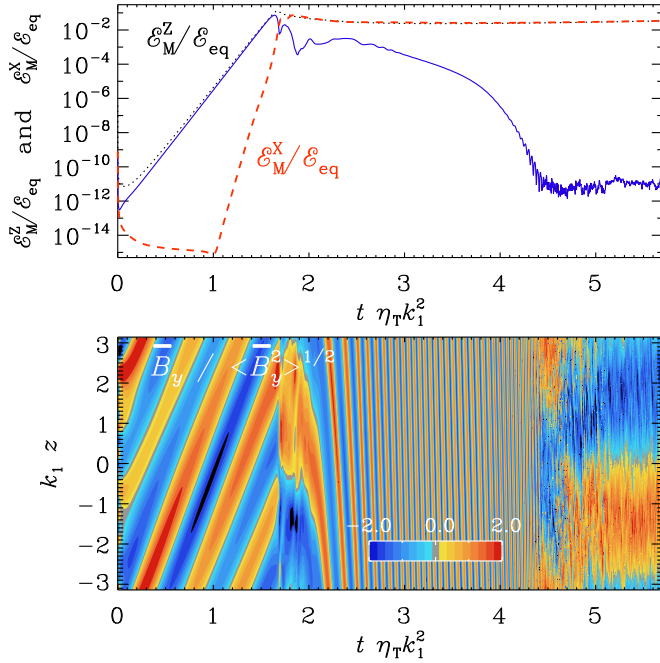


Figure 4. Time dependence of \mathcal{E}_M (dotted black line), \mathcal{E}_M^Z (solid blue line), and \mathcal{E}_M^X (dashed red line), all normalized by $\mathcal{E}_M^{\text{eq}}$, and \bar{B}_y vs. t and z for a fratricidal dynamo (Run F) with $C_\alpha = 1$, $C_\Omega = 150$, $q = -3/2$ (positive shear), and $B_{\text{eq}} \rightarrow \infty$ (no α quenching). Here, \bar{B}_y has been normalized by its instantaneous rms values so as to see the dynamo wave during the early exponential growth phase and also during the late decay phase.

3.1. Fratricidal and Suicidal Mean-field Dynamics

Here, we show that both fratricidal and suicidal dynamos can also occur in a mean-field context; see Figures 4 and 5. The α^2 sibling is here possible because $C_\alpha > L_z/L_x = 0.5$. This is shown in Figure 4, where we plot \mathcal{E}_M^Z and \mathcal{E}_M^X versus time, and \bar{B}_y versus t and z . In the following, this case is referred to as Run F. We see that \mathcal{E}_M^Z grows exponentially, starting from a weak seed magnetic field. The zt diagram in Figure 4 shows the usual dynamo waves. When the dynamo approaches saturation, \mathcal{E}_M^X also begins to grow exponentially, but at a rate that it is much larger than the growth rate of \mathcal{E}_M^Z . When \mathcal{E}_M^X reaches about $10^{-3}\mathcal{E}_M^{\text{eq}}$, \mathcal{E}_M^Z declines rapidly and is then overtaken by \mathcal{E}_M^X . At that moment, the dynamo waves cease and a new transient commences with a rapidly varying time dependence, but at a very low amplitude; see the zt diagram of Figure 4 for $2.5 < t\eta_T k_1^2 < 4.5$.

For $C_\alpha < 0.5$, the α^2 sibling with $\mathcal{E}_M^X \neq 0$ is impossible. Surprisingly, it turned out that the $\alpha\Omega$ dynamo can then still be killed by a secondary \mathcal{E}_M^X , but such a state with $\mathcal{E}_M^X \neq 0$ cannot be sustained and decays on an ohmic timescale; see Figure 5 for Run B. It is therefore an example of a suicidal dynamo. We see that \mathcal{E}_M^X decays toward zero, and that the dynamo wave then just disappears. By that time, \mathcal{E}_M^Z has already become very small and has disappeared within the noise.

3.2. Comparison of Positive and Negative Shear

In our fully nonlinear simulations, it is difficult to say whether the MRI was important and had any particular effect. Unlike an actual physical system, a simulation allows us in principle to identify the effect of each term in the equations by modifying it artificially. Shear is of course crucial for the MRI,

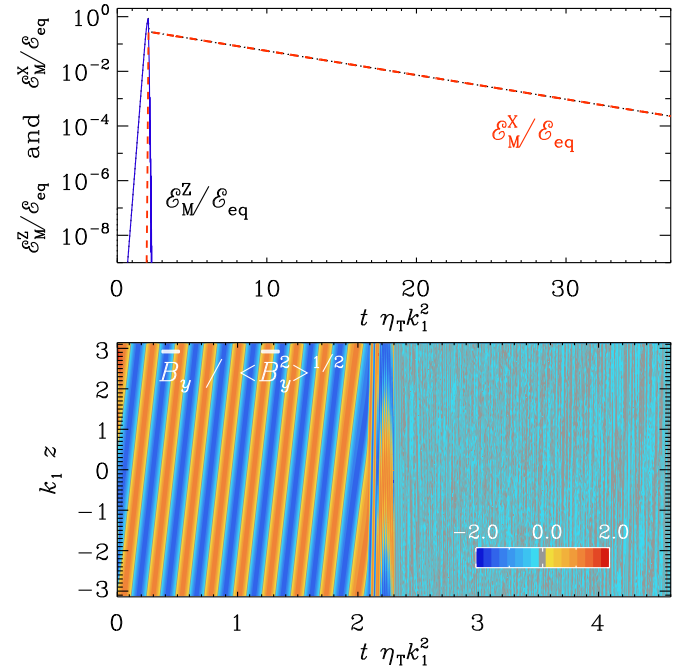


Figure 5. Similar to Figure 4, but for a suicidal dynamo with $C_\alpha = 0.49$ and $C_\Omega = 7.5$ (Run B).

but shear is also crucial for the Ω effect. In our Cartesian system, however, dynamos with prescribed shear and no other dynamics from the momentum equation have analogous properties, i.e., the same rms values of the magnetic field components and relative phase shifts between them, which transform in a known way (H. Yoshimura 1975, 1976; M. Stix 1976). Thus, to identify the effect of the MRI, it is convenient to compare solutions for positive and negative shear. In Figure 6, we plot the time evolutions of \mathcal{E}_M , \mathcal{E}_M^X , and \mathcal{E}_M^Z for Runs C–G with different values of C_α and C_Ω , as well as periodic and vertical field boundary conditions. We see that, regardless of the boundary conditions, the cases with negative shear, where the MRI is possible, tend to have less magnetic energy than the cases with positive shear.

Various parameters related to the flow of energy are summarized in Table 1. We see that W_L is positive, i.e., magnetic energy goes into kinetic energy. This is typical of the MRI and has been found previously for turbulent MRI dynamos (A. Brandenburg et al. 1995). But we also see that whenever C_Ω is negative and the MRI is excited, W_M , W_K , ϵ_M , ϵ_K , and in most cases also W_L are much larger than for positive values of C_Ω , when the MRI does not operate. In the latter case, when only the standard Ω effect operates, W_K is often even negative. Note also that W_P is not given, because its value is very small. Likewise, $\dot{\mathcal{E}}_M$ and $\dot{\mathcal{E}}_K$ are small and not listed, but are still included in the calculation of the total

$$\text{gain} = W_M + W_K + W_\alpha + W_P \quad (9)$$

and

$$\text{loss} = \epsilon_M + \epsilon_K + \dot{\mathcal{E}}_M + \dot{\mathcal{E}}_K. \quad (10)$$

Both the total gain and the total loss balance each other nearly perfectly. In Table 1, we also give the nondimensional growth rate, $\tilde{\lambda} \equiv \lambda/\eta_T k_1^2$, where $\lambda = d \ln \bar{B}_{\text{rms}}/dt$ is the physical growth rate.

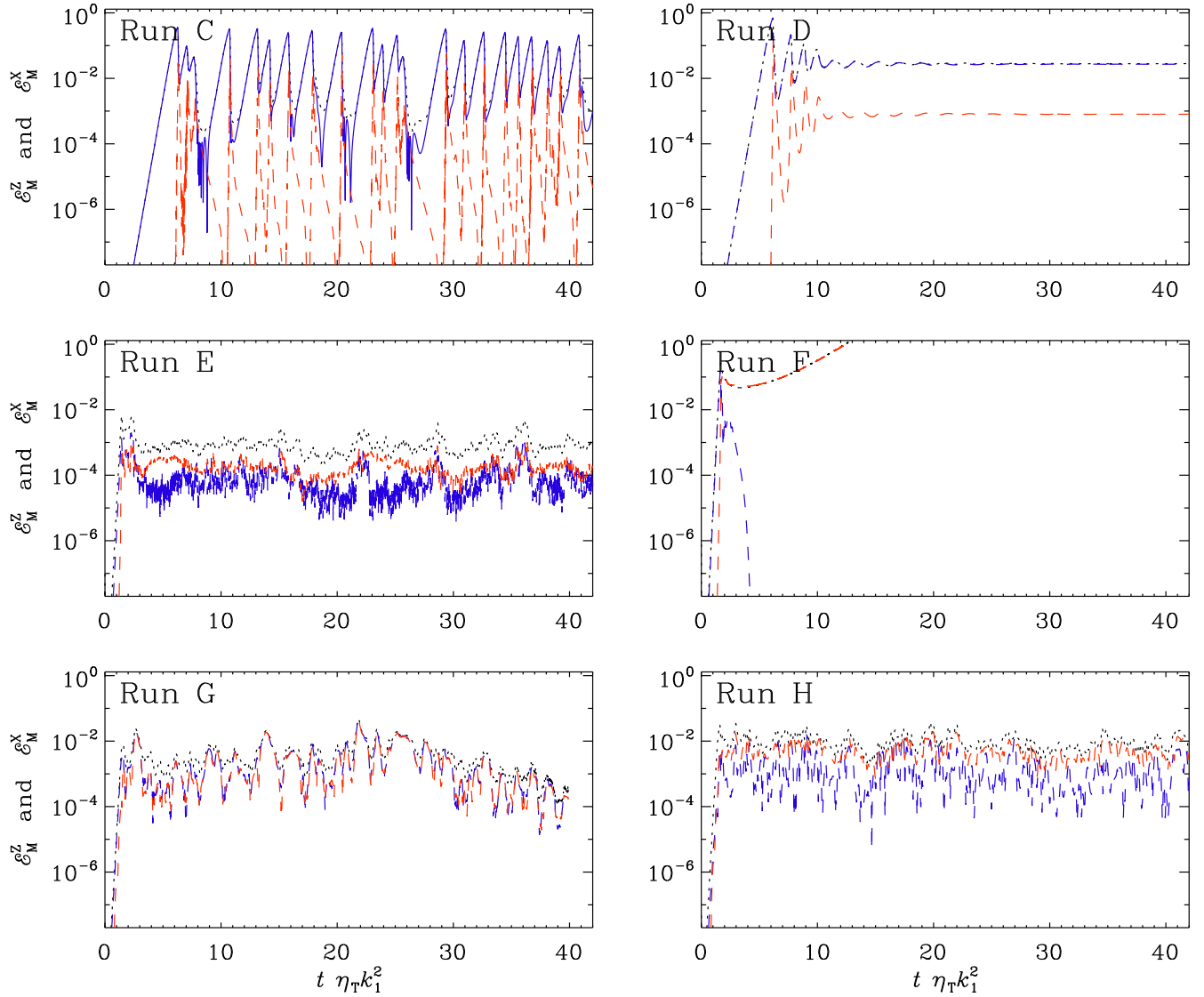


Figure 6. Comparison of solutions for $C_\Omega < 0$ (Runs C, E, and G; left panels) and $C_\Omega > 0$ (Runs D, F, and H; right panels) for periodic boundary conditions (top and middle) and vertical field boundary conditions (bottom). As in the upper panels of Figures 4 and 5, \mathcal{E}_M (dotted black line), \mathcal{E}_M^Z (solid blue line), and \mathcal{E}_M^X (dashed red line), normalized by \mathcal{E}_M^Z , are shown vs. t .

Interestingly, the ratio ϵ_K/ϵ_M , which is known to scale with the microphysical magnetic Prandtl number in direct numerical simulations of forced turbulence (A. Brandenburg 2014), varies widely in the present mean-field calculations. It is less than unity, and often much less than unity. On the other hand, not much is known about the scaling of this dissipation ratio for MRI-driven turbulence. In the old simulations of A. Brandenburg et al. (1995), this ratio was found to be even slightly larger than unity. Given that we present only a coarse coverage of a fairly large parameter space in the Rädler diagram, it is possible that there are some relationships that cannot presently be discerned.

3.3. Magnetic Field Structures

It is instructive to inspect the magnetic field structures of individual snapshots. This is shown in Figure 7, where we present visualizations of field lines in the x - z plane together with a color-scale representation of \bar{B}_y for Runs C–H. In our two-dimensional case, field lines are shown as contours of \bar{A}_y . Runs C and D have a predominantly vertical dependence,

which was already indicated by the dominance of \mathcal{E}_M^Z over \mathcal{E}_M^X in Figure 6. As we have seen before, the MRI operates in Run C, causing some residual x dependence in the field, manifested by the wavy pattern.

Run F is the complete opposite of Run D, because now there is only a pure x dependence. Again, this was also already indicated in Figure 6 through the dominance of \mathcal{E}_M^X over \mathcal{E}_M^Z . This dramatic difference is explained by the value of $C_\alpha = 1$, which is now large enough for an α^2 dynamo with an x extent to be excited.

For negative shear, on the other hand, Runs C and E also show a change from a predominantly z -dependent field for small values of C_α (Run C) to a predominantly x -dependent field for large values of C_α (Run E). However, unlike the fratricidal dynamo for positive shear, where \mathcal{E}_M^Z is completely killed, it is here only partially suppressed; see Figure 6. We could therefore call such a dynamo a narcissistic one. The dominant x dependence of the magnetic field is also evident from Figure 7.

Table 1
Summary of Runs A–Å for $q = 3/2$ and Runs c–j for $q = 1$

Run	BC	$\mathcal{B}_{\text{eq}}^{-1}$	C_α	C_Ω	\mathcal{E}_M	\mathcal{E}_K	W_M	W_K	W_α	W_L	ϵ_M	ϵ_K	Gain	Loss	$\bar{\lambda}$
A	0	0	0.49	−7.5	2.87	0.37	2.5	0.290	0.500	0.16	2.8	0.59	3.3	3.3	0.4
B	0	0	0.49	7.5	1.00	1.93	0.0	0.000	0.490	0.01	0.5	0.01	0.5	0.5	0.4
C	0	0	0.20	−15	1.99	0.08	2.4	0.050	0.085	0.06	2.5	0.23	2.6	2.6	0.2
D	0	0	0.20	15	0.62	0.02	2.0	−0.001	0.080	0.04	2.0	0.04	2.0	2.1	0.2
E	0	0	1.00	−150	0.04	0.27	37.0	10.000	2.000	6.70	33.0	19.00	50.0	50.0	7.5
F	0	0	1.00	150	1.26	0.68	0.3	0.007	1.700	0.37	1.8	0.35	2.0	2.2	7.9
G	1	0	1.00	−150	0.18	0.28	25.0	6.900	1.300	2.50	25.0	8.90	33.0	33.0	7.0
H	1	0	1.00	150	0.24	0.22	8.8	−0.310	0.780	3.50	6.6	3.50	9.2	9.7	7.2
I	1	0	0.20	−150	0.12	0.24	8.1	0.600	0.043	2.30	7.2	3.50	8.8	10.0	2.0
J	1	0	0.20	150	0.33	0.12	3.6	−0.012	0.030	0.73	3.3	0.89	3.6	4.1	1.8
K	0	1	0.49	−7.5	0.15	0.00	1.8	0.000	0.170	0.00	2.0	0.00	2.0	2.0	0.4
L	0	1	0.49	−30	1.07	0.00	2.0	−0.000	0.028	0.00	2.0	0.00	2.0	2.0	1.7
M	0	1	0.49	−75	0.04	0.22	10.0	0.850	0.250	2.80	7.9	4.30	11.0	12.0	3.0
N	0	1	0.49	−150	0.04	0.17	18.0	1.500	0.280	3.00	15.0	6.10	19.0	19.0	4.6
O	0	1	0.49	−300	0.02	0.23	31.0	3.100	0.330	7.80	24.0	14.00	34.0	34.0	7.4
P	0	10	0.49	−30	0.01	0.00	2.0	−0.000	0.027	0.00	2.0	0.00	2.0	2.0	1.6
Q	0	10	0.49	−75	0.03	0.00	2.0	−0.000	0.008	0.00	2.0	0.00	2.0	2.0	3.0
R	0	10	0.49	−300	0.12	0.00	2.1	−0.000	0.001	0.00	2.1	0.00	2.1	2.1	7.4
S	0	10	0.49	−750	0.10	0.00	4.0	0.000	0.010	0.04	4.0	0.04	4.1	4.0	13.4
T	0	10	0.49	−1500	0.09	0.01	7.1	0.008	0.003	0.21	6.9	0.23	7.1	7.0	20.7
U	0	10	0.49	−3000	0.04	0.00	16.0	0.880	0.021	−0.07	16.0	0.86	17.0	19.0	30.9
V	0	100	0.49	−300	0.00	0.00	2.1	−0.000	0.002	0.00	2.1	0.00	2.1	2.1	6.8
W	0	100	0.49	−750	0.00	0.00	2.1	−0.000	0.000	0.00	2.1	0.00	2.1	2.1	11.6
X	0	100	0.49	−1500	0.01	0.00	2.1	−0.000	0.000	0.00	2.1	0.00	2.1	2.1	16.3
Y	0	100	0.49	−3000	0.01	0.00	2.6	−0.000	0.000	0.00	2.3	0.00	2.6	2.6	20.6
Z	0	100	0.49	−7500	0.01	0.00	4.0	0.000	0.000	0.01	3.2	0.01	4.0	4.0	20.8
Å	0	100	0.49	−15000	0.01	0.00	8.5	0.000	0.000	0.02	6.6	0.01	8.5	8.5	19.1
c	0	0	0.20	−15	0.71	7.02	2.4	−0.120	0.084	0.03	2.5	1.60	2.4	3.8	0.2
d	0	0	0.20	15	0.81	0.01	1.9	0.000	0.082	0.04	2.0	0.04	2.0	2.0	0.2
e	0	0	1.00	−150	0.29	1.79	25.0	6.500	1.900	8.50	17.0	15.00	33.0	32.0	7.9
f	0	0	1.00	150	0.89	0.97	0.3	−0.008	1.800	0.64	1.9	0.33	2.0	2.5	7.9
i	1	0	0.20	−150	0.57	0.89	6.5	0.520	0.029	1.90	5.7	2.30	7.0	7.6	2.0
j	1	0	0.20	150	0.38	0.14	3.7	−0.011	0.030	0.85	3.3	0.95	3.8	4.1	1.8

Note. The BC column gives 0 (1) for periodic (vertical field) boundary conditions. For runs without α quenching, we have $\mathcal{B}_{\text{eq}}^{-1} = 0$. \mathcal{E}_M , and \mathcal{E}_K are given in units of $\rho_0 S^2 / k_1^2$. The energy fluxes W_M , W_K , W_α , W_L , ϵ_M , ϵ_K , as well as gain and losses are in units of $\eta_T k_1^2 \mathcal{E}_M$. The last column denotes the nondimensional growth rate $\bar{\lambda} \equiv \lambda / \eta_T k_1^2$.

Runs E and G show predominantly small-scale structures. There is no strong difference between the periodic and nonperiodic runs, except that the field lines are now purely vertical on the boundaries. It is these small-scale structures that are responsible for the enhanced dissipation and ultimately for the decreased efficiency of the dynamo process in the presence of the MRI.

Run H also displays small-scale structures, but these are not related to the MRI, which is absent in this run with positive shear. Here, the existence of small-scale structures is probably related to the presence of boundaries in the z -direction. They lower the excitation conditions for dynamo action with magnetic field dependence in the z -direction, but there could also be other reasons for the existence of small-scale structures in this case.

In Table 1, we also give the results of runs (Runs c–f, as well as i and j) where $q = 1$ instead of $3/2$ but S is unchanged, so Ω is then chosen to be $3/2$. These runs are otherwise similar to Runs C–F, as well as I and J, respectively.

3.4. Simulations with Vertical Boundary Conditions

Next, we study the mean magnetic field evolution for simulations with vertical field boundary conditions in the z -direction. The resulting zt diagrams are shown in Figure 8 for Runs I and J with $C_\Omega = -150$ and $+150$, respectively, using $C_\alpha = 1$. Note that during the early kinematic phase there is clear evidence for dynamo waves migrating in the negative (positive) z -direction for negative (positive) values of C_Ω .

Comparing Runs F and G in Table 1, they have the same parameters, but Run G has vertical field boundary conditions. We see that W_K is much larger in Run G than in Run F. Also W_L is significantly larger in Run G, but the difference is here not quite as large. This is presumably caused by the existence of small-scale structures in Run G, while Run F has essentially only a one-dimensional field structure at late times.

3.5. Transition from Ω Effect to MRI

When C_Ω is small enough, the turbulent magnetic diffusivity may be too large for the MRI to be excited, as the magnetic

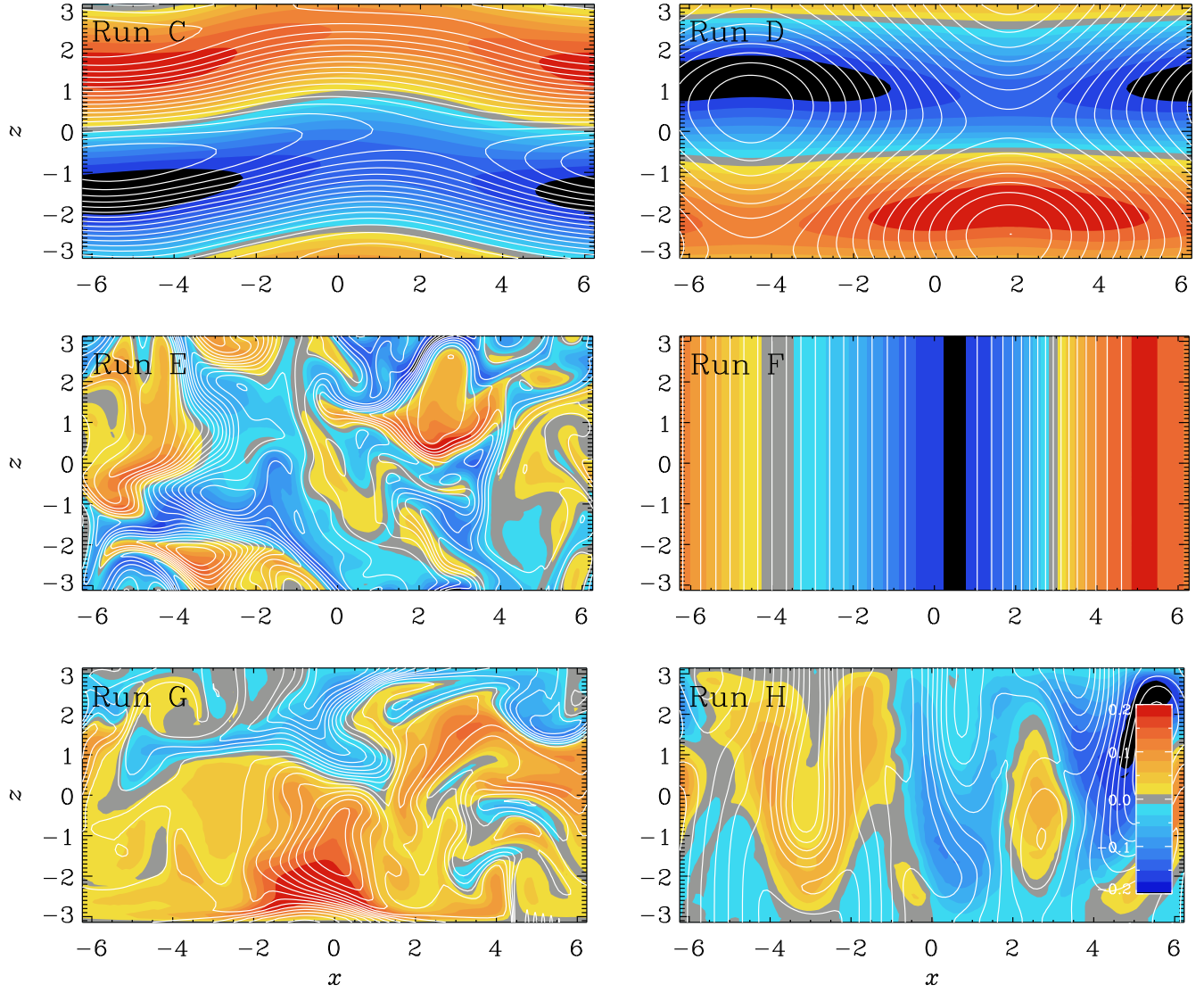


Figure 7. Visualizations of field lines of (\bar{B}_x, \bar{B}_z) in the x - z plane on top of a color-scale representation of \bar{B}_y for Runs C–H, where blue (red) shades refer to negative (positive) values.

diffusion rate might exceed the typical growth rate of the instability, which is of the order of Ω . This idea assumes that the magnetic field is held fixed, but this is not true when the magnetic field is still being amplified by dynamo action and saturation by the large-scale Lorentz force has not yet been achieved. Therefore, since the magnetic field might still be growing, it would not be surprising if the MRI occurred even for small values of C_Ω , corresponding to larger magnetic diffusion rates.

To facilitate dynamo saturation at a lower magnetic field strength, and therefore a regime with $C_\Omega < 0$ without MRI, we now invoke α quenching with finite values of B_{eq} . (The case without α quenching corresponds to $B_{\text{eq}} \rightarrow \infty$.) We have performed numerical experiments for different values of B_{eq} and C_Ω . It turns out that for a fixed value of B_{eq} , there is a critical value of C_Ω above which the MRI commences. This is shown in Figure 9, where we plot the mean magnetic energy density versus $-C_\Omega$ (for $C_\Omega < 0$) and a fixed value of $C_\alpha = 0.49$. We see that \mathcal{E}_M increases approximately linearly with $|C_\Omega|$ and has the same value when normalized by the respective value of $\mathcal{E}_M^{\text{eq}}$. Because the normalized values $\mathcal{E}_M/\mathcal{E}_M^{\text{eq}}$

are the same for different values of $|C_\Omega|$ and different values of \mathcal{E}_M , this saturation dependence is a consequence of α quenching. Above a certain value of $|C_\Omega|$, however, the increasing trend stops and \mathcal{E}_M begins to decline with increasing values of $|C_\Omega|$. We associate this with the onset of the MRI.

The MRI onset occurs for smaller values of $|C_\Omega|$ when B_{eq} is large. This is understandable, because for large values of B_{eq} , α quenching commences only for stronger magnetic fields. Therefore, magnetic field saturation can be accomplished by the MRI before α quenching would be able to act. From the inset of Figure 9, we find quantitatively

$$C_\Omega^{\text{crit}} \approx 30 B_{\text{eq}}^{-1}. \quad (11)$$

Thus, although $C_\Omega < 0$, the standard Ω effect is expected to operate in the range

$$2/C_\alpha \lesssim |C_\Omega| \lesssim C_\Omega^{\text{crit}}, \quad (12)$$

and the MRI is only possible for values of $|C_\Omega|$ larger than C_Ω^{crit} .

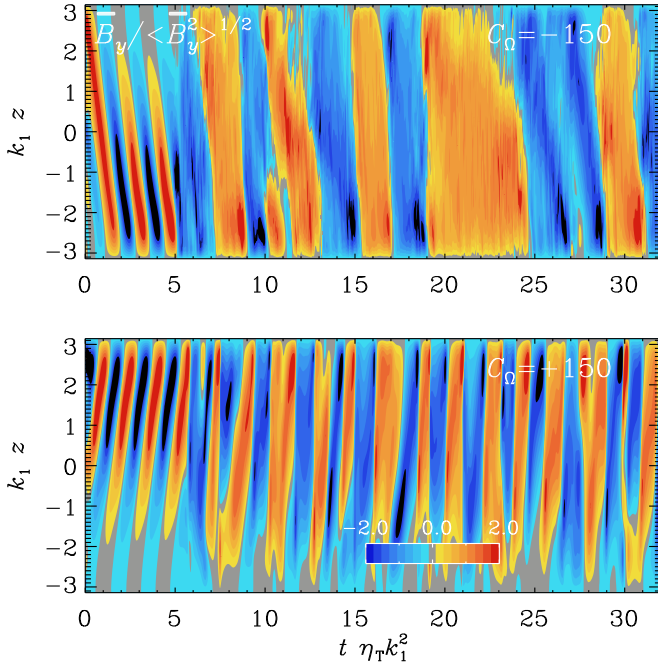


Figure 8. Mean magnetic field evolution in a k_1 - z diagram for simulations with vertical field boundary conditions in the z -direction for Runs I and J with $C_\Omega = -150$ (upper panel) and $C_\Omega = +150$ (lower panel), respectively, using $C_\alpha = 0.2$.

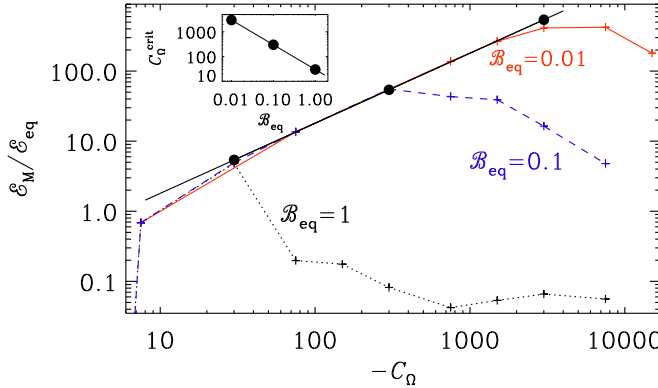


Figure 9. Dependence of $\varepsilon_M / \varepsilon_M^{\text{eq}}$ on C_Ω for $B_{\text{eq}} = 1$ (black dotted line), 0.1 (blue dashed line), and 0.01 (red solid line) using $C_\alpha = 0.49$ in all cases. The black solid line denotes $\varepsilon_M / \varepsilon_M^{\text{eq}} = 0.18 |C_\Omega|$ and the filled circles on this line denote the approximate values where ε_M departs from the linearly increasing trend with $|C_\Omega|$. The inset shows the dependence of C_Ω^{crit} on B_{eq} .

3.6. Comparison with Earlier Work

Let us now discuss whether the MRI might have been excited in previously published work. Hydromagnetic models with α and Λ effects were considered by A. Brandenburg et al. (1992) using spherical geometry. The sign of C_Ω was determined by the sign of the Λ effect. Their C_Ω is defined based on the stellar radius R and can therefore not directly be compared with the C_Ω used in the present work. Also, given that the differential rotation emerges as a result of the Λ effect and is already affected by the magnetic field, their C_Ω is an output parameter.

In their Run T5 of model A−, they found $C_\Omega = -474$, while for their Run T7 of model A+, they found $C_\Omega = +939 \dots +1010$. The magnetic field in this model was oscillatory, which explains the existence of a range of C_Ω .

Table 2

Summary of Solar Estimates for Some Nondimensional Parameters

Depth	B_{eq}^{-1}	C_Ω	$\varepsilon_M / \rho_0 S^2$
7 Mm	0.3	0.3	6
37 Mm	9	9	0.006

To address the question whether the MRI was operational in their model A−, we use the fact that the resulting kinetic energy is large for negative shear when there is shear, compared to the case of positive shear; see Section 3.2. A. Brandenburg et al. (1992) specified the decadic logarithms and found a kinetic energy of $\varepsilon_K = 10^{2.40}$ for their model A− and $\varepsilon_K = 10^{1.65 \dots 1.74}$ for their model A+. This suggests that the MRI was operational in their model A−. Note also that $|C_\Omega|$ was smaller in their Run T5 compared to Run T7. If the driving of kinetic energy were related only to the magnitude of the shear, one would expect the opposite trend. This confirms that the increased kinetic energy in model A− was indeed due to the MRI.

To decide about the excitation of the MRI, we can also estimate their effective value of $v_A k_1 / \Omega$. Using $v_A \approx \sqrt{2\varepsilon_M / \rho_0} \approx 150$, $k_1 = 2\pi / 0.3R \approx 20$, $\Omega = \text{Ta}^{1/2} \eta_T / 2R^2 \approx 2700$, where $\text{Ta} = 3 \times 10^7$ is the turbulent Taylor number, and $\text{Pr}_M = 1$, we find $v_A k_1 / \Omega \approx 1$, which is consistent with the MRI being excited.

3.7. Estimates for the Sun

Let us now estimate some relevant parameters for the Sun. A similar comparison was already presented by G. M. Vasil et al. (2024). For the MRI to be excited, the Alfvén frequency, $\omega_A = v_A k$, must not exceed the rotational shear frequency, $\sqrt{2q} \Omega$, but must also be larger than the turbulent diffusion rate, $\eta_T k^2$, so

$$\eta_T k^2 < \omega_A < \sqrt{2q} \Omega. \quad (13)$$

For the solar NSSL, we have $q = -\partial \ln \Omega / \partial \ln \varpi = 1$ (A. Barekat et al. 2014). For k , we estimate $k \approx 1/\ell$, where ℓ is the local mixing length, which is also approximately equal to the depth, $R - r$, where R is the solar radius and r is the local radius; see Table 2 for a summary of some nondimensional parameters.

In Figure 10, we plot the dependence of ω_A on the depth $R - r$, where the radial dependence of ℓ and ρ has been obtained from the solar mixing length model of H. C. Spruit (1974). Here, we also present estimates of $\eta_T k^2$, where we assume either a constant η_T ($3 \times 10^{12} \text{ cm}^2 \text{ s}^{-1}$) or we use the result of S. Sur et al. (2008):

$$\eta_T = u_{\text{rms}} / 3k. \quad (14)$$

Both estimates show a similar dependence on depth. The value $\eta_T = 3 \times 10^{12} \text{ cm}^2 \text{ s}^{-1}$ is motivated by a similar one for the turbulent heat diffusivity; see V. N. Krivodubskii (1984). G. M. Vasil et al. (2024) also adopted turbulent viscosities and magnetic diffusivities, which they specified as $10^{-6} R^2 \Omega_0 \approx 1.5 \times 10^{10} \text{ cm}^2 \text{ s}^{-1}$. This value, which is 200 times smaller than our estimates above, corresponds to the orange line in Figure 10.

Using for the mean field of the Sun $\bar{B}_{\text{rms}} = 300 \text{ G}$ (A. Brandenburg 2005b; G. M. Vasil et al. 2024), we have

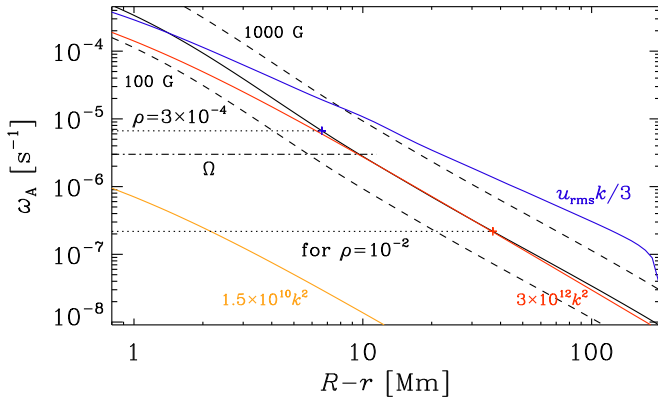


Figure 10. Depth dependence of the Alfvén frequency for $\bar{B}_{\text{rms}} = 300$ G (solid black line) using the mixing length model of H. C. Spruit (1974). Also shown are the values for $\bar{B}_{\text{rms}} = 1000$ G and $\bar{B}_{\text{rms}} = 100$ G (upper and lower dashed lines), as well as $u_{\text{rms}}k/3$ (blue), $3 \times 10^{12} \text{ cm s}^{-1}$ (red line), and $1.5 \times 10^{10} \text{ k}^2 \text{ cm s}^{-1}$ (orange line). The horizontal dotted lines correspond to depths of 7 Mm (where $\rho = 3 \times 10^{-4} \text{ s}^{-1}$) and 40 Mm (where $\rho = 10^{-2} \text{ s}^{-1}$), and $\Omega = 3 \times 10^{-6} \text{ s}^{-1}$ marks the solar angular velocity.

$v_A = 50 \text{ m s}^{-1}$ and $\omega_A = 7 \times 10^{-6} \text{ s}^{-1}$ at a depth of 7 Mm where $\rho \approx 3 \times 10^{-4} \text{ g cm}^{-3}$, and $v_A = 8 \text{ m s}^{-1}$ and $\omega_A = 2 \times 10^{-7} \text{ s}^{-1}$ at a depth of 40 Mm where $\rho \approx 10^{-2} \text{ g cm}^{-3}$. These values bracket the value of Ω , so the MRI might be viable somewhere in this range. However, different estimates for the turbulent diffusion rate $u_{\text{rms}}k/3$ (shown in blue) and $3 \times 10^{12} \text{ cm}^2 \text{ s}^{-1} \text{ k}^2$ (shown in red) lie tightly at ω_A or even exceed it at nearly all depths, making the MRI difficult to excite. Furthermore, if we estimated $k = 2\pi/\ell$ instead of just $1/\ell$, ω_A would attain much higher values and the MRI would not be excited.

Before concluding, let us comment on solar estimates for some of the nondimensional parameters defined in Section 2.2. We see from Equation (7) that $\omega_A/\Omega \equiv \mathcal{B}_{\text{eq}}^{-1}$. Figure 10 shows that this ratio varies between 3 for $R - r = 6$ Mm and 0.1 for $R - r = 40$ Mm; see also Table 2, where we give $\mathcal{B}_{\text{eq}}^{-1}$ (as in Table 1) along with other nondimensional parameters. Note also that, in the parameter range of interest, we have $\mathcal{B}_{\text{eq}}^{-1} \approx C_\Omega$. This is because for $B_{\text{rms}} = 300$ G, we have $\eta_T k^2 \approx \omega_A$, as was already seen from the agreement between the red and black lines in Figure 10. The nondimensional magnetic energies, $\mathcal{E}_M/\rho_0 S^2$, are given by $\mathcal{B}_{\text{eq}}^2/2q^2$ and lie in the range between 6 (closer to the surface) and 0.006 near the bottom of the NSSL.

4. Conclusions

The MRI can only work with negative shear, i.e., when $C_\Omega < 0$. We find that for our models without α quenching and with $C_\Omega < 0$, i.e., when the MRI can operate, the kinetic energy production (W_K) and dissipation (ϵ_K) are large compared to the case where $C_\Omega > 0$. As discussed in Section 3.6, the models of A. Brandenburg et al. (1992), where no α quenching was included, do show enhanced kinetic energy production for negative shear. This suggests that the MRI might indeed have been operating in those models.

Our work has also shown that the MRI can work even for small shear parameters when the magnetic field strength is limited by the large-scale Lorentz force only. However, mechanisms such as α quenching related to the backreaction of the Lorentz force from the small-scale field can prevent the MRI from occurring for small shear parameters. This α

quenching limits the magnetic field strength to values below the critical one where the magnetic diffusion rate exceeds the growth rate of the MRI.

Finally, we discussed whether or not the MRI could play a role in the Sun. Our estimates suggest that turbulent diffusion is likely too large for the MRI to be excited, but the estimates are uncertain because they depend on the magnetic field strength and the value of the wavenumber. If we assumed it were $2\pi/\ell$, the MRI would definitely be ruled out, while for $k = 1/\ell$, it would be right at the limit for $\bar{B}_{\text{rms}} = 300$ G. This value of the magnetic field strength is also what was considered by A. Brandenburg (2005b), and it is compatible with what was assumed by G. M. Vasil et al. (2024), who discussed values in the range between 100 and 1000 G.

It will be of interest to confront our specific findings based on two-dimensional mean-field calculations with those based on direct three-dimensional simulations. So far, the only paper that discusses such a comparison for the MRI is that of M. S. Väisälä et al. (2014), who demonstrated that the onset of the MRI is consistent with what is expected from mean-field estimates. In those cases, there was an imposed magnetic field, which would now need to be replaced by a dynamo-generated one. A problem in reproducing mean-field results in direct numerical simulations is the strength and coherence of the large-scale magnetic field; see D. W. Hughes (2018) for a critical review. A particularly crucial point is the possibility of what has been referred to as catastrophic quenching; see A. Brandenburg (2018) for another review, and P. J. Käpylä (2025) for a more recent one. A leading candidate for alleviating such quenching is magnetic helicity fluxes, which have been computed in numerous studies since the work of E. T. Vishniac & J. Cho (2001). Those suggest that catastrophic dynamo quenching is alleviated by the shear-induced hemispheric small-scale magnetic helicity fluxes. They have a strong effect, as was recently shown in A. Brandenburg & E. T. Vishniac (2025). It would therefore be of interest to repeat such studies in cases where the MRI is also active.

Acknowledgments





This research was supported in part by the Swedish Research Council (Vetenskapsrådet) under grant No. 2019-04234, the National Science Foundation under grant Nos. NSF PHY-2309135, AST-2307698, and AST-2408411, and NASA grant No. 80NSSC22K0825. We acknowledge the allocation of computing resources provided by the Swedish National Allocations Committee at the Center for Parallel Computers at the Royal Institute of Technology in Stockholm. The authors wish to thank the participants of the Nordita program “Stellar Convection: Modelling, Theory, and Observations” in 2024 August and September and the Munich Institute for Astro, Particle and BioPhysics (MIAPbP), which is funded by the Deutsche Forschungsgemeinschaft (DFG, German Research Foundation) under Germany’s Excellence Strategy – EXC-2094 – 390783311, for many inspiring discussions.

Software and Data Availability

The source code used for the simulations of this study, the PENCIL CODE (Pencil Code Collaboration et al. 2021), is freely available on <https://github.com/pencil-code>. The simulation

setups and corresponding input and reduced output data are freely available on doi: [10.5281/zenodo.15258044](https://doi.org/10.5281/zenodo.15258044).

ORCID iDs

- Q3 Axel Brandenburg  <https://orcid.org/0000-0002-7304-021X>
 Gustav Larsson  <https://orcid.org/0009-0008-4918-3852>
 Fabio Del Sordo  <https://orcid.org/0000-0001-9268-4849>
 Petri J. Käpylä  <https://orcid.org/0000-0001-9619-0053>

Q13

References

- Abramowicz, M., Brandenburg, A., & Lasota, J.-P. 1996, *MNRAS*, **281**, L21
 Balbus, S. A., & Hawley, J. F. 1991, *ApJ*, **376**, 214
 Balbus, S. A., & Hawley, J. F. 1992, *ApJ*, **400**, 610
 Balbus, S. A., & Hawley, J. F. 1994, *MNRAS*, **266**, 769
 Balbus, S. A., & Hawley, J. F. 1998, *RvMP*, **70**, 1
 Barekat, A., Schou, J., & Gizon, L. 2014, *A&A*, **570**, L12
 Brandenburg, A. 2005a, *AN*, **326**, 787
 Brandenburg, A. 2005b, *ApJ*, **625**, 539
 Brandenburg, A. 2014, *ApJ*, **791**, 12
 Brandenburg, A. 2018, *JPIPh*, **84**, 735840404
 Brandenburg, A., Elstner, D., Masada, Y., & Pipin, V. 2023, *SSRv*, **219**, 55
 Brandenburg, A., Jennings, R. L., Nordlund, Å., et al. 1996, *JFM*, **306**, 325
 Brandenburg, A., & Käpylä, P. J. 2007, *NJPh*, **9**, 305
 Brandenburg, A., Moss, D., Rüdiger, G., & Tuominen, I. 1991, *GApFD*, **61**, 179
 Brandenburg, A., Moss, D., & Tuominen, I. 1992, *A&A*, **265**, 328
 Brandenburg, A., Nordlund, A., Stein, R. F., & Torkelsson, U. 1995, *ApJ*, **446**, 741
 Brandenburg, A., & Ntormousi, E. 2023, *ARA&A*, **61**, 561
 Brandenburg, A., Rädler, K.-H., Rheinhardt, M., & Käpylä, P. J. 2008, *ApJ*, **676**, 740
 Brandenburg, A., & Sokoloff, D. 2002, *GApFD*, **96**, 319
 Brandenburg, A., & Subramanian, K. 2005, *PhR*, **417**, 1
 Brandenburg, A., Tuominen, I., Moss, D., & Rüdiger, G. 1990, *SoPh*, **128**, 243
 Brandenburg, A., & Vishniac, E. T. 2025, *ApJ*, **984**, 78
 Bushby, P. J., Käpylä, P. J., Masada, Y., et al. 2018, *A&A*, **612**, A97
 Cattaneo, F. 1999, *ApJL*, **515**, L39
 Chan, K. L., Sofia, S., & Mayr, H. G. 1987, in *The Internal Solar Angular Velocity*, ed. B. R. Durney & S. Sofia, Vol. 137 (Dordrecht: Reidel), 347
 Dikpati, M., & Charbonneau, P. 1999, *ApJ*, **518**, 508
 Fuchs, H., Rädler, K. H., & Rheinhardt, M. 1999, *AN*, **320**, 129
 Gierasch, P. J. 1974, *ApJ*, **190**, 199
 Gressel, O. 2010, *MNRAS*, **405**, 41
 Hawley, J. F., & Balbus, S. A. 1991, *ApJ*, **376**, 223
 Hawley, J. F., & Balbus, S. A. 1992, *ApJ*, **400**, 595
 Hawley, J. F., Gammie, C. F., & Balbus, S. A. 1996, *ApJ*, **464**, 690
 Herault, J., Rincon, F., Cossu, C., et al. 2011, *PhRvE*, **84**, 036321
 Hubbard, A., Rheinhardt, M., & Brandenburg, A. 2011, *A&A*, **535**, A48
 Hughes, D. W. 2018, *JPIPh*, **84**, 735840407
 Hughes, D. W., & Proctor, M. R. E. 2009, *PhRvL*, **102**, 044501
 Ivanova, T. S., & Ruzmaikin, A. A. 1977, *SvA*, **21**, 479
 Kagan, D., & Wheeler, J. C. 2014, *ApJ*, **787**, 21
 Käpylä, P. J. 2025, *LRSP*, **22**, 3
 Käpylä, P. J., Korpi, M. J., & Brandenburg, A. 2008, *A&A*, **491**, 353
 Karak, B. B., & Brandenburg, A. 2016, *ApJ*, **816**, 28
 Kippenhahn, R. 1963, *ApJ*, **137**, 664
 Kitchatinov, L. L. 2016, *AstL*, **42**, 339
 Kitchatinov, L. L. 2023, *AstL*, **49**, 754
 Kitchatinov, L. L., & Rüdiger, G. 1995, *A&A*, **299**, 446
 Köhler, H. 1970, *SoPh*, **13**, 3
 Krause, F., & Rädler, K.-H. 1980, *Mean-Field Magnetohydrodynamics and Dynamo Theory* (Oxford: Pergamon Press)
 Krivodubskii, V. N. 1984, *SvA*, **28**, 205
 Lebedinskii, A. I. 1941, *AZh*, **18**, 10
 Leighton, R. B. 1969, *ApJ*, **156**, 1
 Lesur, G., & Ogilvie, G. I. 2008, *A&A*, **488**, 451
 Malkus, W. V. R., & Proctor, M. R. E. 1975, *JFM*, **67**, 417
 Masada, Y. 2011, *MNRAS*, **411**, L26
 Masada, Y., & Sano, T. 2014, *ApJL*, **794**, L6
 Meneguzzi, M., & Pouquet, A. 1989, *JFM*, **205**, 297
 Menou, K., Balbus, S. A., & Spruit, H. C. 2004, *ApJ*, **607**, 564
 Moffatt, H. K. 1978, *Magnetic Field Generation in Electrically Conducting Fluids* (Cambridge: Cambridge University Press)
 Nordlund, A., Brandenburg, A., Jennings, R. L., et al. 1992, *ApJ*, **392**, 647
 Parfrey, K. P., & Menou, K. 2007, *ApJL*, **667**, L207
 Parker, E. N. 1979, *Cosmical Magnetic Fields: Their Origin and Their Activity* (Oxford: Clarendon Press)
 Pencil Code Collaboration, Brandenburg, A., Johansen, A., et al. 2021, *IOSS*, **6**, 2807
 Pipin, V. V. 2017, *MNRAS*, **466**, 3007
 Pipin, V. V., & Kosovichev, A. G. 2019, *ApJ*, **887**, 215
 Rädler, K. H. 1986, *AN*, **307**, 89
 Reboul-Salze, A., Guilet, J., Raynaud, R., & Bugli, M. 2022, *A&A*, **667**, A94
 Rempel, M. 2006, *ApJ*, **647**, 662
 Rincon, F., Ogilvie, G. I., & Proctor, M. R. E. 2007, *PhRvL*, **98**, 254502
 Rüdiger, G. 1980, *GApFD*, **16**, 239
 Rüdiger, G., & Hollerbach, R. 2004, *The Magnetic Universe: Geophysical and Astrophysical Dynamo Theory* (Weinheim: Wiley)
 Rüdiger, G., Küker, M., & Tereshin, I. 2014, *A&A*, **572**, L7
 Rüdiger, G., & Spahn, F. 1992, *SoPh*, **138**, 1
 Rüdiger, G., & Tuominen, I. 1991, in *IAU Coll. 130, The Sun and Cool Stars. Activity, Magnetism, Dynamos*, ed. I. Tuominen, D. Moss, & G. Rüdiger (Heidelberg: Springer), 172
 Schmidt, W. 1982, *GApFD*, **21**, 27
 Schou, J., Antia, H. M., Basu, S., et al. 1998, *ApJ*, **505**, 390
 Schüssler, M. 1979, *A&A*, **72**, 348
 Spruit, H. C. 1974, *SoPh*, **34**, 277
 Spruit, H. C. 2011, in *The Sun, the Solar Wind, and the Heliosphere*, ed. M. P. Miralles & J. Sánchez Almeida, Vol. 4 (Berlin: Springer), 39
 Stix, M. 1974, *A&A*, **37**, 121
 Stix, M. 1976, *A&A*, **47**, 243
 Stone, J. M., Hawley, J. F., Gammie, C. F., & Balbus, S. A. 1996, *ApJ*, **463**, 656
 Sur, S., Brandenburg, A., & Subramanian, K. 2008, *MNRAS*, **385**, L15
 Tuominen, I., Brandenburg, A., Moss, D., & Rieutord, M. 1994, *A&A*, **284**, 259
 Urpin, V. A. 1996, *MNRAS*, **280**, 149
 Väisälä, M. S., Brandenburg, A., Mitra, D., Käpylä, P. J., & Mantere, M. J. 2014, *A&A*, **567**, A139
 Vasil, G. M., Lecoanet, D., Augustson, K., et al. 2024, *Natur*, **629**, 769
 Vishniac, E. T., & Cho, J. 2001, *ApJ*, **550**, 752
 Wasiutynski, J. 1946, *ApNr*, **4**, 1
 Wheeler, J. C., Kagan, D., & Chatzopoulos, E. 2015, *ApJ*, **799**, 85
 Yoshimura, H. 1975, *ApJ*, **201**, 740
 Yoshimura, H. 1976, *SoPh*, **50**, 3
 Zeldovich, Y. B., Ruzmaikin, A. A., & Sokoloff, D. D. 1983, *Magnetic Fields in Astrophysics*, Vol. 3 (New York: Gordon and Breach)
 Zweibel, E. 2024, *Natur*, **629**, 762

Q14